

***Final Draft***  
of the original manuscript:

Schnubel, D.; Huber, N.:

**Retardation of fatigue crack growth in aircraft aluminium alloys  
via laser heating – Numerical prediction of fatigue crack growth**

In: Computational Materials Science (2012) Elsevier

DOI: [10.1016/j.commatsci.2012.07.047](https://doi.org/10.1016/j.commatsci.2012.07.047)

# Retardation of fatigue crack growth in aircraft aluminium alloys via laser heating - Numerical prediction of fatigue crack growth

D. Schnubel<sup>a,\*</sup>, N. Huber<sup>a</sup>

<sup>a</sup>*Institute of Materials Research, Materials Mechanics,  
Helmholtz-Zentrum Geesthacht, 21502 Geesthacht, Germany*

---

## Abstract

The presented study discusses a quantitative numerical approach for predicting the fatigue crack growth in AA2198-T8 C(T)100 specimens containing one line of laser heating. By heating the with a defocused laser residual stresses are introduced and the fatigue crack growth is retarded. The developed methodology, which investigates coupling of the structural process simulation, the extraction of the total stress intensity  $K_{\text{tot}}$  and the prediction of the resulting fatigue crack growth rates by an empirical crack growth law is stepwise validated on the basis of experimental results. The prediction is found to be highly accurate. Special attention needs to be given to the quality of the process simulation results because the prediction of fatigue crack growth is highly sensitive to the results obtained in this simulation step.

*Keywords:* Damage tolerance, Residual stress, Fatigue crack growth, Numerical fracture mechanics, Stress intensity factors, Numerical modelling, Welding simulation

---

\*Corresponding author

*Email address:* [dirk.schnubel@hzg.de](mailto:dirk.schnubel@hzg.de), Phone: +49 4152 87-2637, Fax: +49 4152 87-2549 (D. Schnubel)

*URL:* <http://www.hzg.de> (D. Schnubel)

## Nomenclature

$x, y, z$	position coordinates
$T$	temperature
$t$	time
$\delta_{ij}$	Kronecker delta
$\epsilon$	strain tensor
$\epsilon_{eq}^p$	cumulative plastic strain
$u$	displacement vector
$\sigma$	stress tensor
$\sigma_{eq}$	von Mises stress
$Q$	heat flux density
$Q_0$	heat source amplitude
$v_y$	heat source travelling speed
$\alpha$	thermal expansion coefficient
$E$	Young's modulus
$C, m, n$	material constant of the Walker Equation
$c$	specific heat
$\nu$	Poisson's ratio
$\rho$	density
$\sigma_{ys}$	yield stress
$\lambda$	thermal conductivity
$a$	Crack length
$da/dN$	fatigue crack growth rate
$F_{appl}$	applied load
$G_{tot}$	total energy release rate
$K_{tot}$	total stress intensity factor
$\Delta K_{tot}$	total stress intensity factor range
$R_{tot}$	total stress intensity ratio
$N$	number of load cycles
BM	name prefix for base material results or area with base material properties
EXP	name suffix for experimental results
FEM	finite element method, also name suffix for numerical prediction results
HZ	heating zone
HAZ	heat affected zone
LH	name prefix for laser heating results
MVCCT	Modified Virtual Crack Closure Technique

## 1. Introduction

As was demonstrated in an experimental study on the laser heating of AA2198-T8 specimens [1], residual stresses induced in metallic structures can have a significant impact on fatigue crack growth. Considering the growing interest in advanced manufacturing technologies for the production of metallic integral airframe structures, such as laser beam welding or friction stir welding [2, 3], this issue gained special attention [4–6] because residual stresses are an unavoidable side effect of these technologies [7, 8]. Hence, because precise predictions of fatigue crack growth are required for damage tolerant design, several recent studies have addressed the prediction of fatigue crack growth in integral aircraft aluminium structures including residual stress effects [4–6]. The approach that has found common acceptance consists of the following steps [4, 6, 9–19]:

- Measurement of the component of the residual stresses that acts perpendicular to the crack growth direction.
- Extraction of the residual stress intensity factor  $K_{\text{res}}$  attributable to internal stresses using, for example, the finite element method (FEM) or the weight function method.
- Calculation of the total stress intensity  $K_{\text{tot}} = K_{\text{res}} + K_{\text{appl}}$  as the sum of  $K_{\text{res}}$  and the applied stress intensity  $K_{\text{appl}}$  using the law of superposition.
- Calculation of the fatigue crack growth rate  $da/dN$  by using  $K_{\text{tot}}$  in an empirical crack growth law, such as the Walker Equation.

This general approach shows good results but has two major limitations that need to be addressed. For cracks growing through compressive residual stress fields, nonlinear contact corrections are needed to prevent a physically unsound overlapping of the crack faces during the calculations [9]. Hence, the application of the superposition law is no longer valid. The underlying effects and their impact on the predicted fatigue crack growth rates have been discussed in an earlier study [20]. In addition to issues regarding the numerical approach, residual stress measurements are costly and difficult to perform for complexly shaped or large specimens, and they normally deliver only specific components of the stress tensor for the specific case that is being examined.

The study presented by Jang et al. [21] provided major input for the development of an extended prediction methodology, since it described a strategy to predict the observed fatigue crack growth retardation due to heating induced residual stresses for steel specimens on basis of numerical process simulation results. However, the crack closure based fracture mechanics analysis used does not describe the complex opening behaviour of the crack faces in the residual stress field physically sound. Therefore, the achieved prediction results only showed a qualitative agreement with the measurement results.

Another study pointing into a similar direction was published very recently [22]. Here also structural process simulation was coupled with subsequent mechanical simulations for the calculation of  $K_{\text{res}}$  in a steel butt-weld. However, the resulting crack growth rates were only predicted for one crack length under different applied loads, the crack tip was situated in an area of tensile residual stresses and the predicted crack growth rates were not validated experimentally.

Motivated by these studies the extended methodology shown in Fig. 1 was developed, consisting of the following steps:

1. Use of a FE based process simulation to predict the transient heating temperature field as well as the heating induced residual stresses and distortions.
2. Extraction of the total stress intensity factor  $K_{\text{tot}}$  in a fracture mechanics analysis using the MVCCT approach. In this analysis step the loaded model with predicted heating residual stresses and distortions is incrementally cut open and a contact condition is added continuously for the newly generated crack faces.
3. Calculation of the fatigue crack growth rate  $da/dN$  by using the extracted  $K_{\text{tot}}$  in an empirical crack growth law.

The implementation of this approach was realised using the programming language Python for embedding the two commercial FE codes Sysweld and Abaqus.

## 2. Prediction Methodology

Figure 2 shows the specimen geometry and coordinate system, which are identical to those used in [1], where the results of the experimental investigation on laser heating of AA2198-T8 C(T)100 specimens were presented in detail.

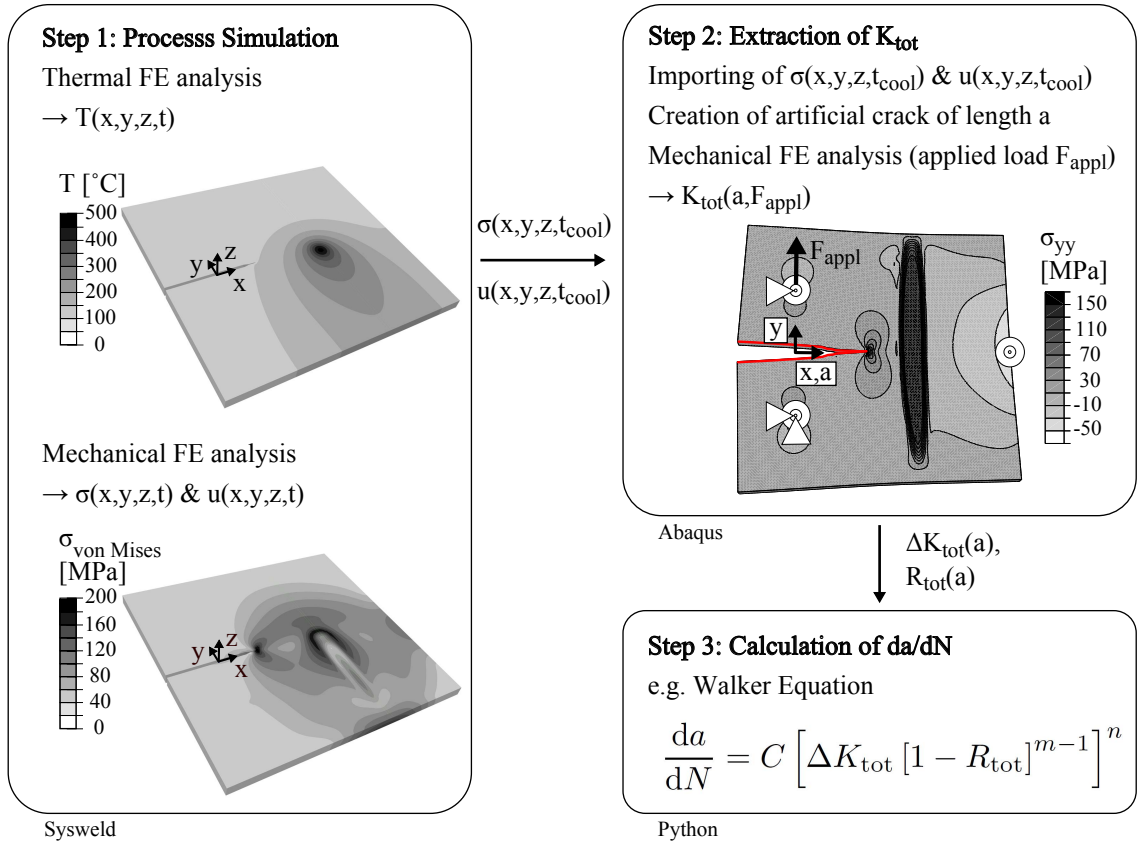


Figure 1: Steps in the extended approach with temperature field  $T(x, y, z, t)$ , residual stress field  $\sigma(x, y, z, t)$ , displacement field  $u(x, y, z, t)$ , cooling time  $t_{cool}$ , crack length  $a$ , applied load  $F_{appl}$ , total stress intensity factor  $K_{tot}(a, F_{appl})$ , total stress intensity factor range  $\Delta K_{tot}(a)$ , total stress intensity ratio  $R_{tot}(a)$  and fatigue crack growth rate  $da/dN$ .

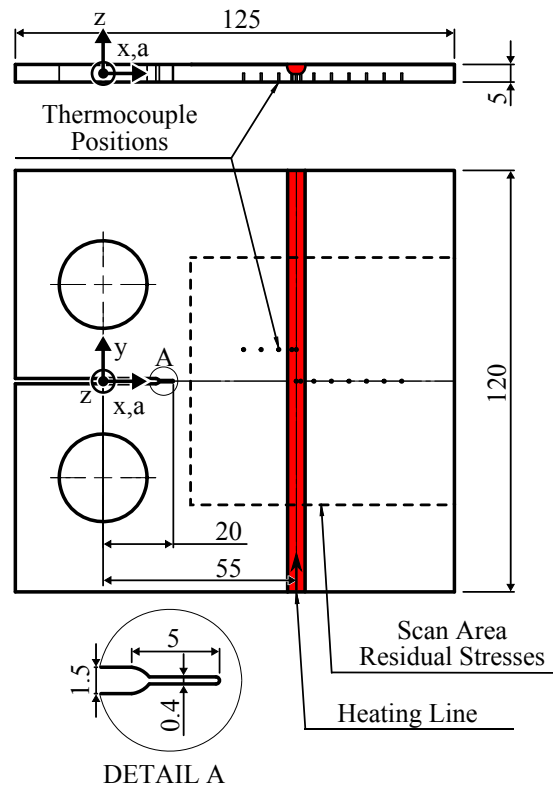


Figure 2: Sketch of the specimen/model dimensions and coordinate system definitions as used also in the experimental study [1]. All measures are given in millimetres. The origin of the  $z$ -coordinate is located at the middle of the specimen thickness.

### 2.1. Step 1: Process simulation

To predict heating-induced residual stresses, a coupled thermal and mechanical FE analysis was conducted. Thus, the influence of the temperature on the mechanical response of the structure is accounted for by including the thermal strains attributable to thermal expansions in the mechanical analysis. However, coupling in the other direction, from the mechanical analysis to the thermal analysis, has not been included [23]. This approach is commonly used for structural simulations of welding processes [24–26]. A thorough overview of the topic is presented, for example, by Radaaj in [24]. For further orientation, [25, 27] also provide some general discussion of the impact of specific simplifications and modelling strategies on the achievable quality of the results.

Although much research has been conducted in the past decades on the simulation of steel welding, few studies have been published on its application to aluminium aerospace alloys. However, in [28–30], for example, friction stir welding of aerospace aluminium alloys was investigated. In [26, 31–36], the resulting distortions and residual stresses after laser beam welding of aluminium T-joints were predicted. In [37, 38], the fusion welding of AA2024 butt joints was studied, and the impact of the testing conditions used to gain the needed temperature-dependent material properties on the prediction results was discussed.

#### 2.1.1. FE mesh

Figure 3 shows the FE mesh used for the process simulation and the extraction of  $K_{\text{tot}}$ . The mesh consists of approximately 40000 linear solid elements and 50000 nodes, and it has the outer dimensions of the C(T)100 specimens used for the experimental studies (see Fig. 2). As shown in Fig. 3, the specimen was modelled as a single piece of material, and for simplicity, no fixture holes were modelled.

#### 2.1.2. Thermal FE analysis

For the thermal analysis, a pure heat conduction model including heat sinks and sources was used. The governing differential equation is given as follows [23]:

$$\rho(T) c(T) \frac{\partial T}{\partial t} - \mathbf{div} (\lambda(T) \mathbf{grad} T) - Q = 0 \quad (1)$$

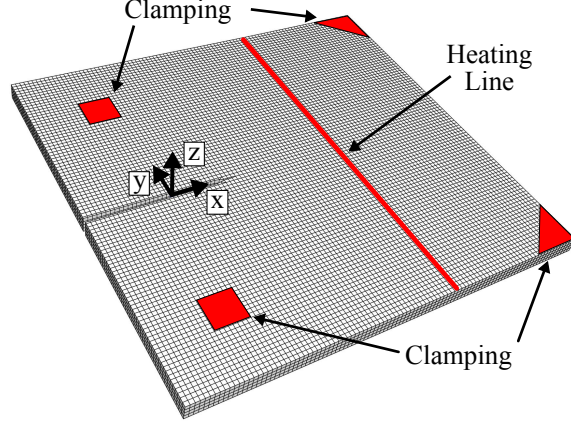


Figure 3: FE mesh built for the thermal and mechanical process simulation. The position of the heating line in the thermal analysis and the areas for the clamping in the mechanical analysis are indicated.

where are  $T$  the temperature,  $c$  the temperature-dependent specific heat,  $\rho$  the temperature-dependent density,  $\lambda$  the temperature-dependent thermal conductivity and  $Q$  the temperature- and/or time-dependent heat flux density (heat sources, boundary conditions).

The heat flux density into the model  $Q_{in}$  has been modelled as a user-defined Goldak ellipsoid volume heat source and can be expressed as a function of the space coordinates  $x, y, z$  and time  $t$ :

$$Q_{in}(x, y, z, t) = Q_0 \exp\left(-\frac{(y - y_0 - v_y t)^2}{A^2} - \frac{(x - x_0)^2}{B^2} - \frac{(z - z_0)^2}{C^2}\right) \quad (2)$$

where are  $Q_0$  the heat source amplitude,  $x_0, y_0, z_0$  the start position of the heat source centre,  $A, B, C$  the heat source shape parameters and  $v_y$  the travelling speed of the heat source in  $y$ -direction.

The heat exchange between model surface and environment was defined as a combination of convective and radiative heat loss [23]:

$$Q_{out}(x_s, y_s, z_s, T) = -h_c(T - T_a) - \sigma_r \epsilon_r (T^4 - T_a^4) \quad (3)$$

where are  $x_s, y_s, z_s$  the surface coordinates,  $T$  the absolute surface temperature,  $T_a$  the absolute ambient temperature,  $h_c$  the coefficient of convective thermal exchange,  $\sigma_r$  the Stefan Boltzmann constant and  $\epsilon_r$  the thermal emissivity.

### 2.1.3. Mechanical FE analysis

For the mechanical analysis, elasto-plastic material behaviour with isotropic hardening and an additive decomposition of the total strain increment  $d\epsilon$  into an elastic strain increment  $d\epsilon^e$ , plastic strain increment  $d\epsilon^p$  and thermal strain increment  $d\epsilon^{\text{th}}$  was assumed [23, 39]:

$$d\epsilon = d\epsilon^e + d\epsilon^p + d\epsilon^{\text{th}} \quad (4)$$

The thermal strain increment  $d\epsilon^{\text{th}}$  is expressed in terms of the thermal expansion coefficient  $\alpha$  and the temperature increment  $dT$  [23, 39]:

$$d\epsilon_{ij}^{\text{th}} = \alpha_{ij} dT \delta_{ij} \quad (5)$$

where is  $\delta_{ij}$  the Kronecker delta.

During the calculations, the thermal strains are updated for each time step on the basis of the results of the thermal analysis.

### 2.1.4. Material properties and boundary conditions

An important conclusion in the literature [26, 38] is that taking into account changes in the precipitation state attributable to the thermal history and the resultant local softening leads only to very slight changes in the predicted residual stresses in the weld area of single pass aluminium welds. Therefore, these effects were neglected in the conducted simulations. However, neglecting these effects implies that temperature dependent material properties are used that are representative for the examined process [38].

Figures 4 and 5 show the temperature-dependent material properties used in the process simulation. Because no measurement data were available for the used material AA2198-T8, most of the properties were adopted from the internal Sysweld material database for AlSiMg. Since the temperature-dependent yield stress and thermal conductivity influence the prediction results most [40], for these two properties more realistic values from the literature were used.

The thermal conductivity  $\lambda$  of AA2195 was taken from [28]. AA2195 is like AA2198 also an Al-Li-Cu alloy. The chemical composition of AA2195 shows a similar Li content and approximately one weight percent more Cu compared to AA2198 [41]. Hence, the thermal conductivity of AA2195 should be in the same regime as the one of AA2198.

With regard to the used yield stress data the performed simulations clearly indicated that plastic yielding during laser heating takes place only

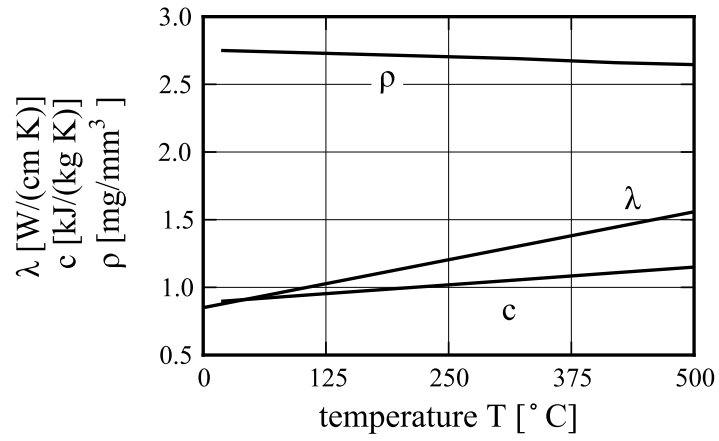
for  $T > 250$  °C. Hence, the assumed yield stress for  $T > 250$  °C governs the development of the residual stresses and not the room temperature values. Unfortunately, no measurement data for AA2198-T8 was available in this temperature range. Therefore, in the performed simulations the temperature-dependent  $\sigma_{ys}$  data published in [37] of the material AA2024-T3 was used instead. Table 1 gives a comparison of literature values for the  $\sigma_{ys}$  of AA2024-T3, AA2198-T8 and AA2195-T8 at different temperatures. At room temperature the yield stress of AA2198-T8 is 150 MPa higher than the one of AA2024-T3. However, it can be expected that this difference is decreasing with increasing temperature as it can be found for the other Al-Li-Cu alloy AA2195-T8. At room temperature the yield stress of AA2195-T8 is even 230 MPa higher than the one of AA2024-T3 while at  $T = 370$  °C only a difference of 9 MPa remains.

Table 1: Comparison of the yield stress of AA2024-T3, AA2198-T8 and AA2195-T8 for room temperature ( $RT$ ) and 370 °C.

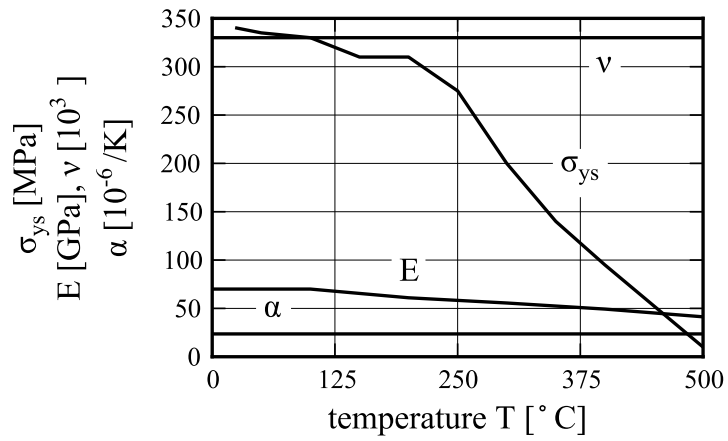
Material	Temperature	$\sigma_{ys}$	Source
AA2024-T3	$RT$	340 MPa	[37]
AA2198-T8	$RT$	490 MPa	[42]
AA2195-T8	$RT$	570 MPa	[43]
AA2024-T3	370 °C	122 MPa	[37]
AA2198-T8	370 °C	-	-
AA2195-T8	370 °C	131 MPa	[44]

Table 2 shows the boundary conditions for the thermal analysis that were adjusted iteratively to fit the thermo couple measurement results. Although the peak temperatures reached in the simulations are dominated by the heat source definition, the fade of the temperature after the heat source has passed is directly related to the heat exchange with the environment.

Because the specimens were clamped onto a table during laser heating, two thermal contact conditions were defined to describe the heat exchange. For the top surface of the specimen ( $z_s > -2.5$  mm), which was only in thermal contact with the surrounding air during laser heating, a value of  $h_c = 25.0$  W/(m<sup>2</sup>K) was assumed. For the bottom surface of the specimen, which was in thermal contact with the table ( $z_s = -2.5$  mm), a higher value of  $h_c = 75.0$  W/(m<sup>2</sup>K) was found to deliver good results.



(a)



(b)

Figure 4: Temperature-dependent material properties used for the (a) thermal and (b) mechanical process simulations.

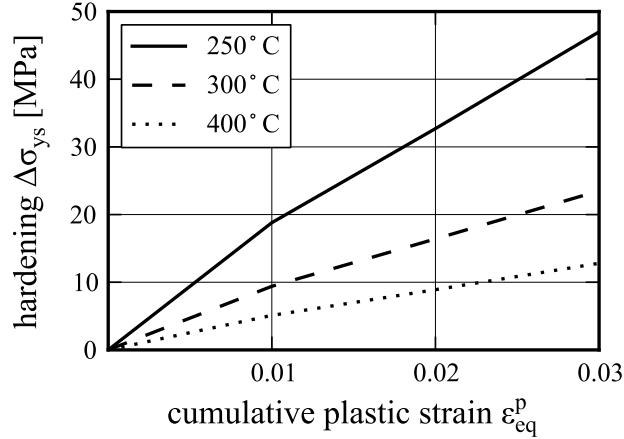


Figure 5: Three of the lookup curves used for the yield stress increase  $\Delta\sigma_{ys}$  attributable to isotropic hardening. The whole data set covers the temperature range  $0\text{ }^\circ\text{C} < T < 500\text{ }^\circ\text{C}$  with nine curves.

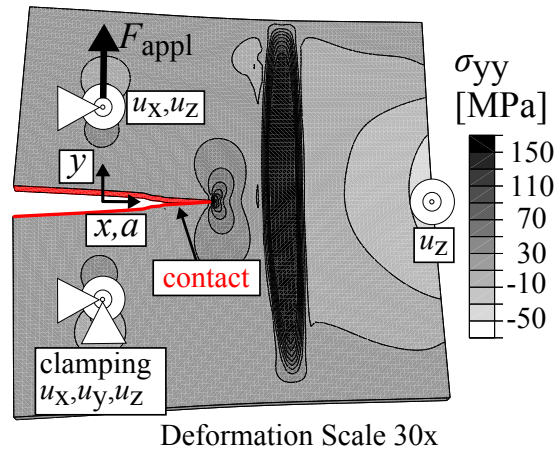
The clamping conditions during laser heating were modelled in the mechanical analysis using elastic constraints on the nodes in the areas marked in Fig. 3 on the top and bottom surfaces of the specimen. The chosen values adopt results published in [45], obtaining a total spring constant of approximately 0.4 kN/mm for each clamping position in each direction.

To estimate the sensitivity of the prediction results with regard to the heat source calibration as well as the thermal conductivity and yield stress data a corresponding sensitivity analysis is given in section 3.

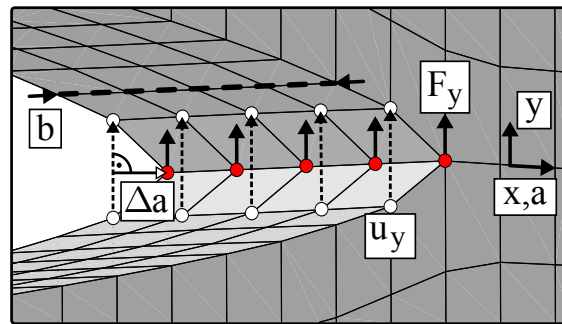
## 2.2. Step 2: Extraction of $K_{tot}$

For the calculation of  $K_{tot}$ , the deformed mesh and the full stress field from the last time step of the process simulation are transferred to the FE code Abaqus. The mechanical restart simulation in Abaqus assumes pure linear elastic material behaviour with a Young’s modulus  $E = 73\text{ GPa}$  and a Poisson’s ratio  $\nu = 0.33$ .

The extraction of  $K_{tot}$  for different crack lengths was realised by cutting the model open along the specified crack path. A hard contact condition was added on the generated crack faces to avoid physically unreasonable overlapping [20]. Figure 6a shows the corresponding model. The displacement boundary conditions and the external load  $F_{appl}$  were applied to single nodes at the specified positions in the mid thickness of the model.



(a)



(b)

Figure 6: (a) Graphic of the mechanical restart simulation model with the applied boundary conditions and (b) schematic view of the extraction of  $K_{tot}$  via the MVCCT approach.

Table 2: Boundary conditions for the thermal analysis

---

$(x_0, y_0, z_0)$	=	(55.0 mm, -60.0 mm, 2.5 mm)
$v_y$	=	3.33 mm/s
$A$	=	4.0 mm <sup>2</sup>
$B$	=	4.0 mm <sup>2</sup>
$C$	=	0.5 mm <sup>2</sup>
$Q_0$	=	26.0 ± 1.0 W/mm <sup>3</sup> (hatched light grey area in result figures)
$h_c$	=	$\begin{cases} 75.0 \text{ W}/(\text{m}^2\text{K}) & , \text{ if } z_s = -2.5 \text{ mm} \\ 25.0 \text{ W}/(\text{m}^2\text{K}) & , \text{ if } z_s > -2.5 \text{ mm} \end{cases}$
$\sigma_r$	=	$5.67 \cdot 10^{-8} \text{ W}/(\text{m}^2 \text{K}^4)$
$\epsilon_r$	=	0.8

---

The Modified Virtual Crack Closure Technique (MVCCT) illustrated in Fig. 6b was used to extract the total energy release rate  $G_{\text{tot}}$  for each crack length using the specimen thickness  $b$ , the nodal cutting forces  $F_y$  of the crack tip nodes and the nodal displacements  $u_y$  of the nodes located on the crack faces at a distance  $\Delta a$  behind the crack tip in Eq. (6). Further details about that approach can be found, for example, in [15, 46, 47]. The total stress intensity factor  $K_{\text{tot}}$  was then calculated using  $G_{\text{tot}}$  in Eq. (7):

$$G_{\text{tot}} = \frac{1}{2 \cdot b \cdot \Delta a} \sum F_y \cdot u_y \quad (6)$$

$$K_{\text{tot}} = \sqrt{G_{\text{tot}} \cdot E} \quad (7)$$

Equation (7) is based on the plane stress condition.

### 2.3. Step 3: Calculation of the fatigue crack growth rate $da/dN$

Under cyclic loading with the maximum applied load  $F_{\text{max}}$  and the minimum applied load  $F_{\text{min}}$ , the conditions at the crack tip can be described using the total stress intensity factor range  $\Delta K_{\text{tot}}$  given in Eq. (8) and the stress intensity factor ratio  $R_{\text{tot}}$  defined in Eq. (9).

The presence of residual stresses can lead to changes in both  $\Delta K_{\text{tot}}$  and  $R_{\text{tot}}$ . Hence, an empirical crack growth law is needed for the prediction of the fatigue crack growth rate  $da/dN$  that is sensitive to both  $\Delta K_{\text{tot}}$  and  $R_{\text{tot}}$ . In this study, the Walker Equation [48] given in Eq. (10) was used.

The number of loading cycles  $N$  for reaching a specific crack length  $a$  was then calculated by the numerical integration of the inverse of the predicted  $da/dN$  as defined in Eq. (11).

$$\Delta K_{\text{tot}} = K_{\text{tot}}(F_{\text{max}}) - K_{\text{tot}}(F_{\text{min}}) \quad (8)$$

$$R_{\text{tot}} = K_{\text{tot}}(F_{\text{min}})/K_{\text{tot}}(F_{\text{max}}) \quad (9)$$

$$da/dN = C [\Delta K_{\text{tot}} [1 - R_{\text{tot}}]^{m-1}]^n \quad (10)$$

$$\int_0^N dN = \int_{a_0}^a \left( C [\Delta K_{\text{tot}} [1 - R_{\text{tot}}]^{m-1}]^n \right)^{-1} da \quad (11)$$

To calibrate the Walker Equation for use with AA2198-T8, five fatigue crack growth tests were performed on five base material specimens (two specimens  $R = 0.01$ , two specimens  $R = 0.1$  and one specimen  $R = 0.7$ ). The resulting best fit for the material constants gave  $C = 1.15 \cdot 10^{-10}$  m/cycle,  $n = 2.80$  and  $m = 0.665$ .

### 3. Results and Discussion

In the following sections, a stepwise validation of the numerical simulation results is conducted on the basis of experimental data [1]. Where needed, the lateral extension of the heating zone (HZ), the heat-affected zone (HAZ) and the areas with base material properties (BM) estimated on basis of the measured micro hardness (see [1] and Fig. 8) are indicated in the figures. Additionally, the sensitivity of the prediction results with regard to the heat source amplitude  $Q_0$ , the temperature-dependent heat conductivity  $\lambda$  and the temperature-dependent yield stress  $\sigma_{\text{ys}}$  is given.

#### 3.1. Step 1: Process simulation

##### 3.1.1. Thermal FE analysis

As stated, the thermal analysis was manually calibrated so that good agreement between measurements and thermal FE analysis results was achieved. Figure 7a presents a comparison of the thermo couple measurements and the simulation results for the nodes at the corresponding positions. Figure 7b presents a comparison of the measured and numerically predicted peak temperatures  $T_{\text{max}}$  during the thermo cycle as a function of the  $x$ -position. As shown, excellent agreement was achieved with the calibrated heat source amplitude  $Q_0 = 26$  W/mm<sup>3</sup>.

To obtain an estimate of the sensitivity of the prediction results on the performed calibration, the variation of the results attributable to a relative change of the key calibration parameter  $Q_0 = 26 \text{ W/mm}^3$  in the range of  $\pm 4 \%$  is indicated in Fig. 7b as a light-grey hatched area. As shown, this variation of  $Q_0$  leads to a moderate shift in the predicted peak temperatures in the middle of the HZ of approximately  $\pm 12 \text{ }^\circ\text{C}$ , what is in the same range as the observed scatter of the measured peak temperatures shown as open symbols in Fig. 7b. The same variation in the peak temperature in the HZ and HAZ can be found for a relative change of the thermal conductivity  $\lambda$  in the range of  $\pm 5 \%$  at constant  $Q_0 = 26 \text{ W/mm}^3$ .

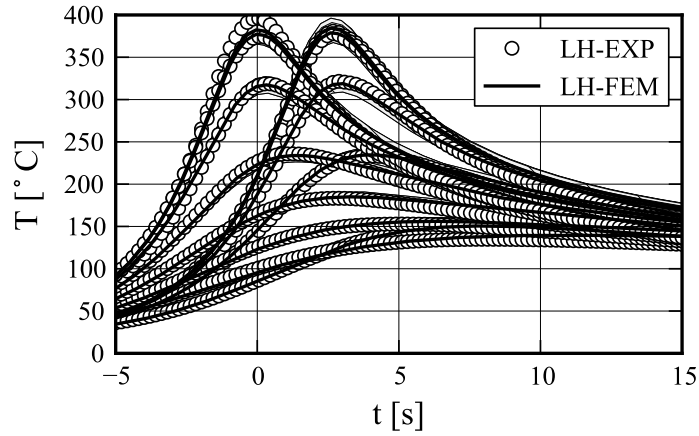
The comparison with the thermo couple measurements shows that the global heat input, the thermal conduction and heat exchange with the environment of the experiment were matched very well by the thermal simulation. However, to obtain reasonable residual stress predictions, the very localised heat input in the heating zone also needs to match the experiment. Therefore, the local heat input for welding simulations is normally calibrated on the basis of the lateral extension of the molten and heat-affected zone, which can be measured directly in optical macro graphs. Because no melting occurred during laser heating, that approach was not possible for the calibration of the laser heating simulation.

However, Fig. 8 shows an overlay of the micro hardness measurement results [1] ( $HV$  colour plot) and selected isothermal contours of the numerically predicted peak temperatures  $T_{\max}$ . Comparing those two quantities seems reasonable because the reduction in hardness is a direct consequence of the changes in the micro structure attributable to the heating cycles [37, 38, 49–51]. The zones with different hardness match the  $T_{\max}$  contours well, indicating that the local heat input into the specimen was also described well by the calibrated thermal model.

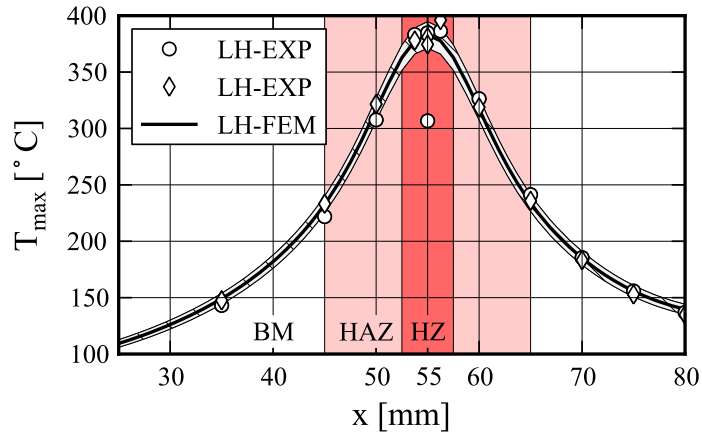
### 3.1.2. Mechanical FE analysis

Figure 9 and Fig. 10 show a comparison of the measured and predicted residual stress differences  $\Delta\sigma = \sigma_{yy} - \sigma_{xx}$ . As shown in Fig. 9, the general pattern is the same for measurements and simulations. The calculated line scans in Fig. 10 reveal that the mechanical simulation based on the calibrated thermal model ( $Q_0 = 26 \text{ W/mm}^3$ ) delivers a reasonable prediction for the residual stresses, even though higher values are predicted especially in the HZ compared with the measurements.

In addition to the stress differences  $\Delta\sigma$ , the numerically predicted longi-



(a)



(b)

Figure 7: Comparison of the thermocouple measurements (LH-EXP) and the results of the thermal FE analysis (LH-FEM) (a) measured and simulated transient temperatures and (b) measured and simulated peak temperatures. The variation of the results is indicated for a relative variation of  $Q_0$  in the range of  $\pm 4\%$  as the hatched light-grey area around the solid black line ( $Q_0 = 26 \text{ W/mm}^3$ ). In HZ and HAZ the same variation width for the peak temperatures was found for a relative change of the thermal conductivity  $\lambda$  in the range of  $\pm 5\%$ .

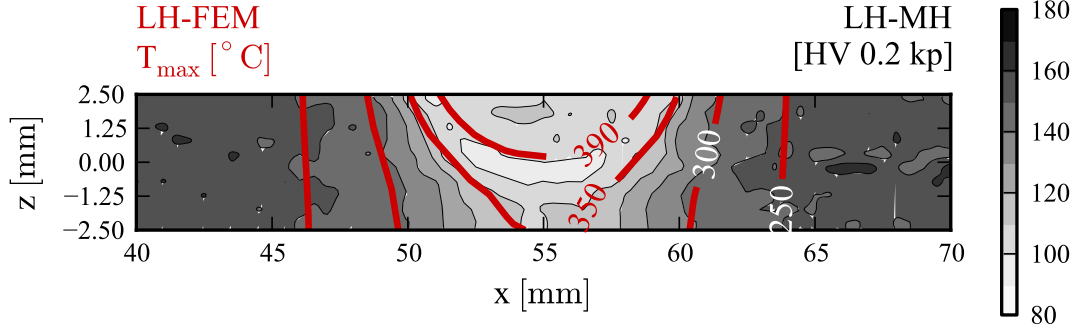


Figure 8: Overlay of the micro hardness measurement results (LH-MH) and the contours of the numerically predicted reached maximum temperatures  $T_{\max}$ .

tudinal stresses  $\sigma_{yy}$  (dashed) and transverse stresses  $\sigma_{xx}$  (dotted) are shown. The amplitude of the transverse stresses  $\sigma_{xx}$  is small compared with that of the longitudinal stresses  $\sigma_{yy}$ . Therefore, the stress difference  $\Delta\sigma$  is dominated by the contribution of  $\sigma_{yy}$ , and both  $\Delta\sigma$  as well as  $\sigma_{yy}$  have a change from negative to positive values at  $x = 49$  mm.

Shown as hatched light-grey area in Fig. 10 is the variation of the predicted  $\Delta\sigma$  attributable to a relative variation of  $Q_0$  in the range of  $\pm 4\%$ ,  $\lambda$  in the range of  $\pm 5\%$  or  $\sigma_{ys}$  in the range of  $\pm 15\%$ , respectively. A variation in the mentioned ranges leads to changes of  $\Delta\sigma$  up to  $\pm 15$  MPa in the HZ, whereas the changes in the BM area are only in the range of  $\pm 3$  MPa.

Based on this sensitivity study it can be stated that already small changes of the process temperature fields (see hatched light-grey area in Fig. 7b) can explain large changes of the tensile residual stress peak in the HZ (see hatched light-grey area in Fig. 10). Or in other words, the observed large differences between predicted and measured  $\Delta\sigma$  in the HZ can be explained by a small, relative variation of the process peak temperatures that is laying in the same range as the observed experimental scatter from the thermocouple measurements.

Alternatively, also an difference between the temperature-dependent  $\sigma_{ys}$  of AA2198-T8 and the used literature values of AA2024-T3 in the range of  $\pm 15\%$  would explain the noted differences between predicted and measured  $\Delta\sigma$ .

However, another aspect to account for is the missing statistics in the residual stress measurement results. Unfortunately, because of the large experimental effort associated with the synchrotron diffraction experiments it was only possible to conduct measurements on one specimen. Hence, the seen differences in predicted and measured residuals stresses should not be over-rated. For clarification and to improve the reliability of the residual stress measurement results, performing measurements on more specimens and with a combination of different measurement methods should be considered for future work.

### 3.2. Step 2: Extraction of $K_{\text{tot}}$

The results of the extraction of  $K_{\text{tot}}(a)$  are shown in the upper graph of Fig. 11 for a model without residual stresses (BM-FEM) as well as for the mapped results from the process simulation of the laser heating process (LH-FEM). In this graph, the upper two curves represent the values for the maximum applied load, and the lower two curves represent the values for the minimum applied load.

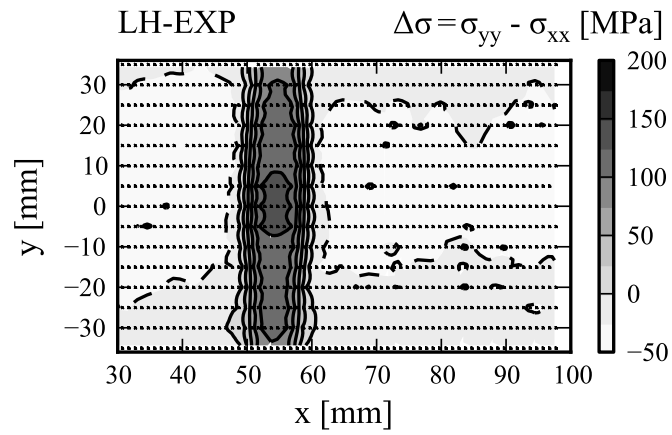
For  $a < 49$  mm, the crack tip is situated in the area of compressive longitudinal stresses  $\sigma_{yy}$  for the simulation with laser heating. Hence,  $K_{\text{tot}}$  is reduced in comparison with the simulations for the base material. Under minimum applied load, the crack faces remain completely closed, as indicated by  $K_{\text{tot}} = 0 \text{ MPa}\sqrt{\text{m}}$ .

After the crack tip enters the area of tensile longitudinal residual stresses  $\sigma_{yy}$  for  $a > 49$  mm,  $K_{\text{tot}}$  begins to increase for both minimum and maximum applied loads, exceeding the corresponding values from the simulations for the base material.

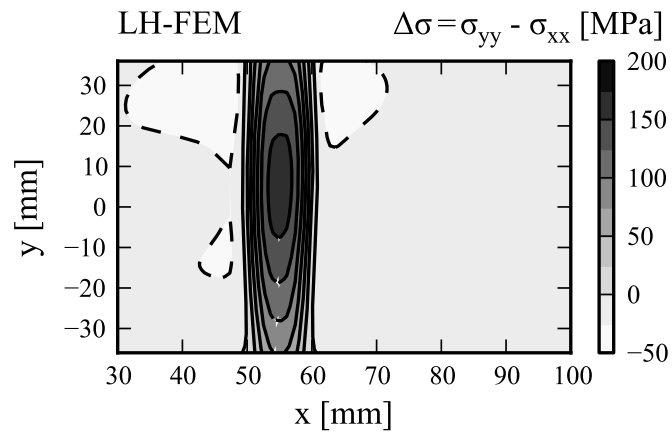
Again, the small variation in the prediction results for a relative variation of  $Q_0$  in the range of  $\pm 4$  %,  $\lambda$  in the range of  $\pm 5$  % or  $\sigma_{ys}$  in the range of  $\pm 15$  % is shown.

### 3.3. Step 3: Calculation of the fatigue crack growth rate $da/dN$

As shown in the lower two graphs of Fig. 11,  $\Delta K_{\text{tot}}$  (see Eq. (8)) and  $R_{\text{tot}}$  (see Eq. (9)) were calculated on the basis of the extracted  $K_{\text{tot}}$ . The modulation of  $K_{\text{tot}}$  caused by the residual stresses reduced  $\Delta K_{\text{tot}}$  in comparison with the base material for all crack lengths.  $R_{\text{tot}}$  became zero when the crack tip was in the area of compressive  $\sigma_{yy}$  and increased to a value of nearly 0.5 in the area of high tensile stresses  $\sigma_{yy}$  (HZ).



(a)



(b)

Figure 9: Comparison of the (a) measured and (b) predicted residual stress differences  $\Delta\sigma = \sigma_{yy} - \sigma_{xx}$ . The numerical results have been averaged through the specimen thickness to allow direct comparison with the measured results.

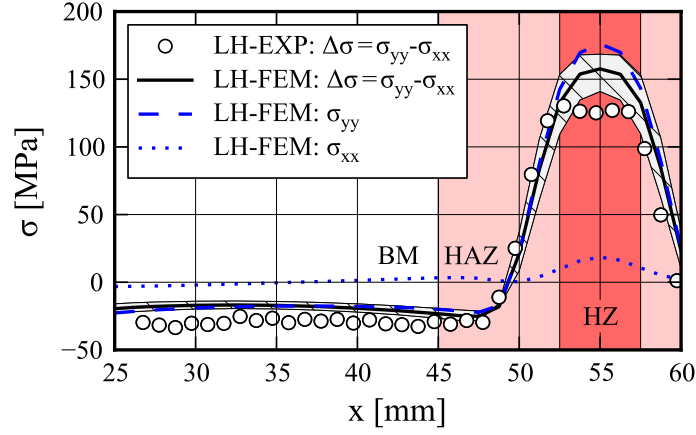


Figure 10: Line scan computed by averaging the area scan data given in Fig. 9 along the  $y$  coordinate for  $-12 \text{ mm} < y < 12 \text{ mm}$ . The measurement results (white markers) and the FE results (solid black line) are shown. Additionally shown are the numerical prediction results for the single stress components are plotted as dashed ( $\sigma_{yy}$ ) and dotted ( $\sigma_{xx}$ ) lines. The hatched light-grey area indicates the variation of the predicted  $\Delta\sigma$  for a relative variation of  $Q_0$  in the range of  $\pm 4 \%$ ,  $\lambda$  in the range of  $\pm 5 \%$  or  $\sigma_{ys}$  in the range of  $\pm 15 \%$ .

The calculated  $\Delta K_{\text{tot}}$  and  $R_{\text{tot}}$  were used in the Walker Equation (see Eq. (10)), with the material constants for AA2198-T8 given in section 2.3, to predict the fatigue crack growth rates  $da/dN$ . A comparison of the prediction results with the measured crack growth rates from the base material specimens (BM-EXP) and the laser-heated specimens (LH-EXP) is given in Fig. 12. As shown, the prediction results fit the experimental data very well. For the base material specimens without residual stresses, this good fit is just a graphical validation of the correct estimation of the Walker Equation constants. The agreement of the prediction and measurement results for the specimens with laser heating shows that the developed approach is able to predict the impact of the induced residual stresses on the fatigue crack growth with high accuracy.

An interesting point is that in contradiction to the general expectation a large change of the maximum tensile residual stresses in the HZ as indicated earlier by the hatched light-grey area in Fig. 10, does only lead to comparatively small changes of the fatigue crack growth rate in the HZ as indicated by the hatched light-grey area in Fig. 12. This is due to the fact

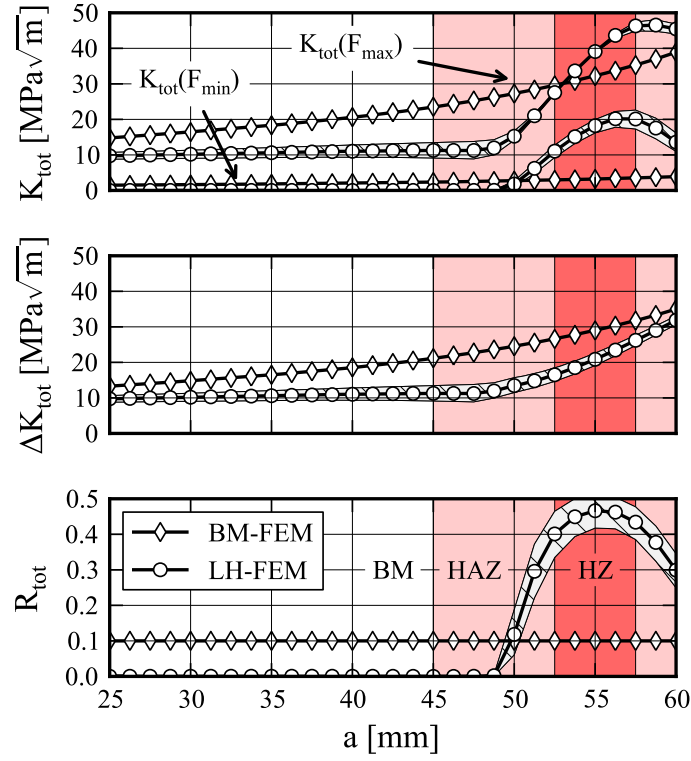


Figure 11: Extracted total stress intensity factor  $K_{tot}$ , total stress intensity factor range  $\Delta K_{tot}$  and total stress intensity factor ratio  $R_{tot}$ . The hatched light-grey areas indicate the variation of the prediction results for a relative variation of  $Q_0$  in the range of  $\pm 4\%$ ,  $\lambda$  in the range of  $\pm 5\%$  or  $\sigma_{ys}$  in the range of  $\pm 15\%$ .

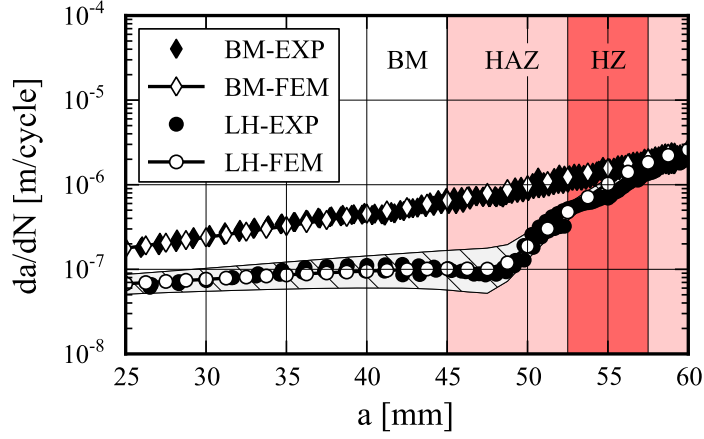


Figure 12: Comparison of the numerically predicted and measured crack growth rates  $da/dN$  as a function of the crack length  $a$ . The hatched light-grey area indicates the variation of the prediction results for a relative variation of  $Q_0$  in the range of  $\pm 4\%$ ,  $\lambda$  in the range of  $\pm 5\%$  or  $\sigma_{ys}$  in the range of  $\pm 15\%$ .

that the tensile residual stresses in the HZ influence mainly  $R_{tot}$  as seen in lower graph of Fig. 11. Compared to  $\Delta K_{tot}$  the influence of  $R_{tot}$  on the crack growth rates is rather small.

The crack length  $a$  as a function of the number of cycles was then calculated as defined in Eq. (11) and also compared with the measurement results as shown in Fig. 13. Here, also a very good agreement between prediction and measurement results was found.

Even though the predicted fatigue crack growth rate in Fig. 12 varies only slightly with the variation of  $Q_0$ ,  $\lambda$  or  $\sigma_{ys}$ , this variation has a substantial impact on the predicted crack growth length  $a(N)$  as indicated by the hatched area in Fig. 13. This effect is caused by the accumulation of the small but systematic prediction uncertainty in  $da/dN$  during the numerical integration. The substantial impact of even slight changes of the process simulation results on the predicted fatigue crack growth highlights that special care needs to be taken to avoid making predictions that are not sufficiently conservative. From this point of view the grey hatched area marked in Fig. 13 can be interpreted as confidence region for the prediction results, since the variation width for the thermal process simulation calibration was derived from the experimentally observed scatter of the thermocouple measurements.

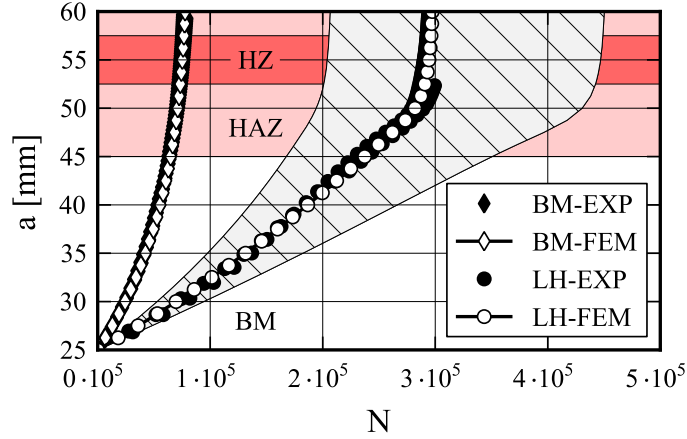


Figure 13: Experimentally measured and predicted crack length  $a$  as a function of the loading cycles  $N$  for the base material specimens and the laser-heated specimens. The hatched light-grey area indicates the variation of the prediction results for a relative variation of  $Q_0$  in the range of  $\pm 4\%$ ,  $\lambda$  in the range of  $\pm 5\%$  or  $\sigma_{ys}$  in the range of  $\pm 15\%$ .

#### 4. Conclusions

An extended approach has been presented using numerical process simulation in conjunction with numerical extraction of stress intensity factors to predict the fatigue crack growth for specimens containing heating-induced residual stresses. The approach has been developed and validated stepwise for the case of AA2198-T8 specimens containing a line of laser heating.

For each step of the validation, good agreement with the measurement results was found. The sensitivity of the prediction results on the calibration of the thermal process simulation analysis and on the used temperature dependent material properties was investigated. Even though the impact on the induced peak temperatures, residual stresses and crack growth rates was comparatively small, a substantial impact on the predicted crack length as a function of the loading cycles was found because here slight deviations integrate over the lifetime. Hence, it can be concluded that the predicted lifetimes are highly sensitive to results of the numerical process simulation, and thus, special care needs to be taken to avoid the possibility of non-conservative prediction results.

The predicted and measured crack growth rates also matched well for the areas that were found to have a changed micro structure (HZ, HAZ) in

the experimental examinations [1]. The predictions did not account for the effects of a changed micro structure on the mechanical properties, which is an indication that the observed retardation effect is mainly induced by residual stresses, and the effects of the changed micro structure are negligible.

It was demonstrated that the proposed approach is capable of predicting with very high accuracy the fatigue crack retardation attributable to laser heating. In future the developed prediction approach can be used for the optimisation of different design parameters, e.g., the line positioning on the specimens via simulations, before beginning broad experimental studies based on trial and error. Especially regarding the application of laser heating on larger specimens or structures, this can be expected to substantially decrease the experimental effort.

Besides, the proposed modelling strategy can be easily adopted for other processes aiming to retard fatigue crack growth by the introduction of compressive residual stresses such as cold expansion or laser shock peening, which can be accomplished by substituting the welding process simulation used in this study with other numerical simulations that deliver a full stress field for the corresponding process.

## Acknowledgements

The authors would like to thank Dr. Waman Vishwanath Vaidya of Helmholtz-Zentrum Geesthacht, Germany, for invaluable discussions on the topic.

- [1] D. Schnubel, M. Horstmann, V. Ventzke, S. Riekehr, P. Staron, T. Fischer, N. Huber, Retardation of fatigue crack growth in aircraft aluminium alloys via laser heating - Experimental proof of concept, *Materials Science and Engineering: A* 546 (2012) 8–14.
- [2] H.-J. Schmidt, Damage tolerance technology for current and future aircraft structures, in: C. Dalle Donne (Ed.), *Proceedings of the 23rd ICAF Symposium of the International Committee on Aeronautical Fatigue*, volume 1, 2005, pp. 1 – 41.
- [3] R. Kocik, T. Vugrin, T. Seefeld, Laserstrahlschweissen im Flugzeugbau: Stand und künftige Anwendungen, in: *Strahltechnik*, volume 28, BIAS, 2006, pp. 15–26.

- [4] X. Zhang, P. Irving, L. Edwards, M. Fitzpatrick, I. Sinclair, J. Lin, D. Yapp, The influence of residual stress on design and damage tolerance of welded aircraft structures, in: C. Dalle Donne (Ed.), Proceedings of the 23rd ICAF Symposium of the International Committee on Aeronautical Fatigue, volume 1, 2005, pp. 265–281.
- [5] L. Edwards, M. E. Fitzpatrick, P. E. Irving, I. Sinclair, X. Zhang, D. Yapp, An integrated approach to the determination and consequences of residual stress on the fatigue performance of welded aircraft structures, *Journal of ASTM International* 3 (2006). Paper ID JAI12547.
- [6] P. Irving, Y. E. Ma, X. Zhang, G. Servetti, S. Williams, G. Moore, J. dos Santos, M. Pacchione, Control of crack growth rates and crack trajectories for enhanced fail safety and damage tolerance in welded structures, in: M. Bos (Ed.), Proceeding of the 25th ICAF Symposium of the International Committee on Aeronautical Fatigue, 2009, pp. 387 – 405.
- [7] P. Staron, W. V. Vaidya, M. Koçak, J. Homeyer, J. Hackius, Residual stresses in laser beam welded butt joints of the airframe aluminium alloy AA6056, *Materials Science Forum* 524-525 (2006) 413–418.
- [8] W. Machold, P. Staron, F. Bayraktar, S. Riekehr, M. Koçak, A. Schreyer, Influence of the welding sequence on residual stresses in laser welded T-joints of an airframe aluminium alloy, *Materials Science Forum* 571-572 (2008) 375–380.
- [9] A. Parker, Stress Intensity Factors, Crack Profiles and Fatigue Crack Growth Rates in Residual Stress Fields, in: J. F. Throop, H. S. Reem-snyder (Eds.), *Residual Stress Effects in Fatigue*, volume ASTM STP 776, ASTM, 1982, pp. 13–31.
- [10] Y.-B. Lee, C.-S. Chung, Y.-K. Park, H.-K. Kim, Effects of redistributing residual stress on the fatigue behavior of SS330 weldment, *International Journal of Fatigue* 20 (1998) 565 – 573.
- [11] H. N. Mahmoud, R. J. Dexter, Propagation rate of large cracks in stiffened panels under tension loading, *Marine Structures* 18 (2005) 265 – 288.

- [12] L. Edwards, Influence of residual stress redistribution on fatigue crack growth and damage tolerant design, *Materials Science Forum* 524-525 (2006) 77–82.
- [13] G. Labeas, I. Diamantakos, Numerical investigation of through crack behaviour under welding residual stresses, *Engineering Fracture Mechanics* 76 (2009) 1691 – 1702.
- [14] C. Liljedahl, J. Brouard, O. Zanellato, J. Lin, M. Tan, S. Ganguly, P. Irving, M. Fitzpatrick, X. Zhang, L. Edwards, Weld residual stress effects on fatigue crack growth behaviour of aluminium alloy 2024-T351, *International Journal of Fatigue* 31 (2009) 1081 – 1088.
- [15] G. Servetti, X. Zhang, Predicting fatigue crack growth rate in a welded butt joint: The role of effective R ratio in accounting for residual stress effect, *Engineering Fracture Mechanics* 76 (2009) 1589 – 1602.
- [16] R. Bao, X. Zhang, N. A. Yahaya, Evaluating stress intensity factors due to weld residual stresses by the weight function and finite element methods, *Engineering Fracture Mechanics* 77 (2010) 2550 – 2566.
- [17] M. Beghini, L. Bertini, Fatigue crack propagation through residual stress fields with closure phenomena, *Engineering Fracture Mechanics* 36 (1990) 379 – 387.
- [18] M. Beghini, L. Bertini, E. Vitale, Fatigue crack growth in residual stress fields: Experimental results and modelling, *Fatigue & Fracture of Engineering Materials & Structures* 17 (1994) 1433 – 1444.
- [19] H. Terada, Stress intensity factor analysis and fatigue behavior of a crack in the residual stress field of welding, *Journal of ASTM International* 2 (2005).
- [20] D. Schnubel, N. Huber, The influence of crack face contact on the prediction of fatigue crack propagation in residual stress fields, *Engineering Fracture Mechanics* 84 (2012) 15–24.
- [21] C. D. Jang, H. C. Song, C. H. Lee, Fatigue life extension of a through-thickness crack using local heating, in: *Proceedings of The Twelfth*

- (2002) International Offshore and Polar Engineering Conference, The International Society of Offshore and Polar Engineers, Kitakyushu, Japan, pp. 224–229.
- [22] C.-H. Lee, K.-H. Chang, Finite element computation of fatigue growth rates for mode I cracks subjected to welding residual stresses, *Engineering Fracture Mechanics* 78 (2011) 2505–2520.
- [23] ESI, SYSWORLD 2010 Technical Description of Capabilities, 2010.
- [24] D. Radaaj, *Welding residual stresses and distortion: Calculation and measurement*, DVS Verlag, 2003.
- [25] L. Lindgreen, Modelling for residual stresses and deformations due to welding - Knowing what isn't necessary to know, in: H. Cerjak, H. Bhadeshia (Eds.), *Mathematical Modelling of Weld Phenomena*, volume 6, Institute of Materials, Minerals and Mining, 2001, pp. 491–518.
- [26] M. Zain-ul-Abdein, D. Nelias, J.-F. Jullien, F. Boitout, L. Dischert, X. Noe, Finite element analysis of metallurgical phase transformations in AA 6056-T4 and their effects upon the residual stress and distortion states of a laser welded T-joint, *International Journal of Pressure Vessels and Piping* 88 (2011) 45 – 56.
- [27] P. Dong, Residual stresses and distortions in welded structures: a perspective for engineering applications, *Science and Technology of Welding and Joining* 10 (2005) 389–397.
- [28] Y. J. Chao, X. Qi, W. Tang, Heat transfer in friction stir welding Experimental and numerical studies, *Journal of Manufacturing Science and Engineering* 125 (2003) 138–145.
- [29] D. Richards, P. Prangnell, S. Williams, P. J. Withers, Global mechanical tensioning for the management of residual stresses in welds, *Materials Science & Engineering A* 489 (2008) 351–362.
- [30] D. Y. Yan, A. P. Wu, J. Silvanus, Q. Y. Shi, Predicting residual distortion of aluminum alloy stiffened sheet after friction stir welding by numerical simulation, *Materials & Design* 32 (2011) 2284 – 2291.

- [31] M. A. Zaeem, M. Nami, M. Kadivar, Prediction of welding buckling distortion in a thin wall aluminum T joint, *Computational Materials Science* 38 (2007) 588 – 594.
- [32] M. Zain-ul-Abdein, D. Nelias, J.-F. Jullien, D. Deloison, Prediction of laser beam welding-induced distortions and residual stresses by numerical simulation for aeronautic application, *Journal of Materials Processing Technology* 209 (2009) 2907 – 2917.
- [33] D. Schnubel, M. Koçak, P. Staron, Mechanical tensioning - An innovative method to improve the damage tolerance of laser welded aluminium skin-stringer joints in airframes, in: *Proceedings of the 3rd European Conference on Aero-Space Science (EUCASS)*, Versailles, 2009, pp. 1 – 8.
- [34] D. Schnubel, M. Koçak, P. Staron, Mechanisches Vorspannen - Eine Möglichkeit zur Modifikation schweissinduzierter Verzüge und Eigenspannungen, in: *Proceedings of the SYSWELD Forum 2009*, Weimar, 2009, pp. 266 – 273.
- [35] M. Zain-ul-Abdein, D. Nelias, J.-F. Jullien, D. Deloison, Experimental investigation and finite element simulation of laser beam welding induced residual stresses and distortions in thin sheets of AA 6056-T4, *Materials Science and Engineering: A* 527 (2010) 3025 – 3039.
- [36] M. Zain-ul-Abdein, D. Nelias, J.-F. Jullien, A. I. Wagan, Thermo-mechanical characterisation of AA 6056-T4 and estimation of its material properties using genetic algorithm, *Materials & Design* 31 (2010) 4302 – 4311.
- [37] R. V. Preston, H. R. Shercliff, P. J. Withers, S. D. Smith, Finite element modelling of tungsten inert gas welding of aluminium alloy 2024, *Science and Technology of Welding & Joining* 8 (2003) 10–18(9).
- [38] R. Preston, H. Shercliff, P. Withers, S. Smith, Physically-based constitutive modelling of residual stress development in welding of aluminium alloy 2024, *Acta Materialia* 52 (2004) 4973 – 4983.
- [39] A. F. Bower, *Applied Mechanics of Solids* (<http://solidmechanics.org>), 2009.

- [40] X. K. Zhu, Y. J. Chao, Effects of temperature-dependent material properties on welding simulation, *Computers and Structures* 80 (2002) 967 – 976.
- [41] M. Knüwer, J. Schumacher, H. Ribes, F. Eberl, B. Bes, 2198 - Advanced Aluminium-Lithium Alloy for A350 Skin Sheet Application, in: *Presentation for the 17th AeroMat Conference & Exposition, Seattle, USA, 2006*, pp. 1–27.
- [42] J. Chen, Y. Madi, T. F. Morgeneyer, J. Besson, Plastic flow and ductile rupture of a 2198 Al-Cu-Li aluminum alloy, *Computational Materials Science* 50 (2011) 1365–1371.
- [43] P. Lequeu, F. Eberl, S. Jambu, T. Warner, A. Danielou, B. Bes, Latest generation of Al-Li alloys developed by Alcan Aerospace, in: *Proceedings of the 1st EUCOMAS European Conference on Materials and Structures in Aerospace, VDI Verlag, 2008*, pp. 1–8.
- [44] W. Arbegast, Using Gleeble flow stress data to establish optimum FSW processing parameters in aluminum alloys, in: *Presentation for the 13th AeroMat Conference & Exposition, Orlando, Florida USA, 2002*, pp. 1 – 39.
- [45] M. F. Zäh, S. Lutzmann, A. Schober, S. Schulz, Sensitivität des Bauteilverzugs beim Schweißen in Abhängigkeit verschiedener Einspannbedingungen, in: *Proceedings of the SYSWELD Forum 2009, Weimar, 2009*, pp. 274 – 283.
- [46] V. Richter-Trummer, S. Tavares, P. Moreira, M. de Figueiredo, P. de Castro, Residual stress measurement using the contour and the sectioning methods in a MIG weld : Effects on the stress intensity factor, *Ciência e Tecnologia dos Materiais* 20 (2008) 115–119.
- [47] R. Krueger, The Virtual Crack Closure Technique: History, Approach and Applications, Technical Report NASA/CR-2002-211628, ICASE Report No. 2002-10, NASA, ICASE, 2002.
- [48] K. Walker, The effect of stress ratio during crack propagation and fatigue for 2024-T3 and 7075-T6, in: *Effects of environment and complex load history on fatigue life, volume STP 462, ASTM, 1970*, pp. 1 – 14.

- [49] Ø. Grong, Metallurgical Modelling of Welding, volume 677 of *Materials Modelling Series*, The Institute of Materials, 1997.
- [50] O. Myhr, Ø. Grong, Process modelling applied to 6082-T6 aluminium weldments - I. Reaction kinetics, *Acta Metallurgica et Materialia* 39 (1991) 2693 – 2702.
- [51] O. Myhr, Ø. Grong, Process modelling applied to 6082-T6 aluminium weldments - II. Applications of model, *Acta Metallurgica et Materialia* 39 (1991) 2703 – 2708.